

Article

Design, Analysis, and Comparison of Electric Vehicle Electric Oil Pump Motor Rotors Using Ferrite Magnet

Huai-Cong Liu

Hwaseong Powertrain R&D Center, Hyundai-Transys, 95, Hyundaikia-ro, Namyang-Eup, Hwaseong-si 18280, Republic of Korea; hcliu@hyundai-transys.com; Tel.: +82-010-3076-9989

Abstract: With the recent proliferation of electric vehicles, there is increasing attention on drive motors that are powerful and efficient, with a higher power density. To meet such high power density requirements, the cooling technology used for drive motors is particularly important. To further optimize the cooling effects, the use of direct oil-cooling technology for drive motors is gaining more attention, especially regarding the requirements for electric vehicle electric oil pumps (EOPs) in motor cooling. In such high-temperature environments, it is also necessary for the EOP to maintain its performance under high temperatures. This research explores the feasibility of using high-temperature-resistant ferrite magnets in the rotors of EOPs. For a 150 W EOP motor with the same stator size, three different rotor configurations are proposed: a surface permanent magnet (SPM) rotor, an interior permanent magnet (IPM) rotor, and a spoke-type IPM rotor. While the rotor sizes are the same, to maximize the power density while meeting the rotor's mechanical strength requirements, the different rotor configurations make the most use of ferrite magnets (weighing 58 g, 51.8 g, and 46.3 g, respectively). Finite element analysis (FEA) was used to compare the performance of these models with that of the basic rotor design, considering factors such as the no-load back electromotive force, no-load voltage harmonics (<10%), cogging torque (<0.1 Nm), load torque, motor loss, and efficiency (>80%). Additionally, a comprehensive analysis of the system efficiency and energy loss was conducted based on hypothetical electric vehicle traction motor parameters. Finally, by manufacturing a prototype motor and conducting experiments, the effectiveness and superiority of the finite element method (FEM) design results were confirmed.

Keywords: EOP; ferrite magnet; surface permanent magnet; interior permanent magnet; spoke-type IPM; finite element method



Academic Editors: Joeri Van Mierlo, Myoung-ho Sunwoo and Namwook Kim

Received: 11 December 2024

Revised: 9 January 2025

Accepted: 14 January 2025

Published: 20 January 2025

Citation: Liu, H.-C. Design, Analysis, and Comparison of Electric Vehicle Electric Oil Pump Motor Rotors Using Ferrite Magnet. *World Electr. Veh. J.* **2025**, *16*, 50. <https://doi.org/10.3390/wevj16010050>

Copyright: © 2025 by the author. Published by MDPI on behalf of the World Electric Vehicle Association. Licensee MDPI, Basel, Switzerland. This article is an open access article distributed under the terms and conditions of the Creative Commons Attribution (CC BY) license (<https://creativecommons.org/licenses/by/4.0/>).

1. Introduction

EOPs play a crucial role in modern vehicles, primarily in the following ways. For traditional fuel vehicles, EOPs are mainly used for starting assistance: during the vehicle startup, the EOP can quickly establish the fuel pressure, helping the engine to start quickly [1,2]. EOPs are also used for lubrication and cooling: they lubricate and cool all types of transmissions, such as automatic transmission (AT), dry or wet dual-clutch transmission (DCT), dedicated hybrid transmission (DHT), continuously variable transmission (CVT), and manual transmission (MT), and reducers, including gears, clutches, and electric drives, as well as providing a lower proportion of the drive (clutches, hydraulic shifting, and hydraulic parking locks) [3–5]. In pure electric vehicles, especially in some high-performance vehicles, EOPs are mainly used to cool and lubricate the motor end-winding coils and reducer gear sets, preventing overheating and wear [6,7]. The design of EOPs needs to consider multiple

key factors to ensure their efficient, reliable, and safe operation. One major issue with the use of electrical products in the engine compartment is that the maximum temperature can reach 130 °C. Compared to general fuel vehicles, the ambient temperature for EOPs is slightly lower, but for some high-performance drive motors with speeds exceeding 16,000 rpm, the coil temperature often exceeds 150 °C to 180 °C [8,9]. Therefore, EOPs must directly spray a cooling medium onto the heat-generating components, such as reducer gears and motor stator end-windings. The structure of the direct oil-cooling system is shown in Figure 1. Excessive coil temperatures can rapidly increase the oil temperature, raising the heat-resistance requirements of the EOP. Therefore, the design of EOPs must consider high-temperature demagnetization under such high temperatures. To further prevent motor demagnetization in high-temperature environments, heavy rare earth elements, including Dy and Tb, must be added to the permanent magnets. However, with the rising prices of rare earth permanent magnets, there are concerns about the stability of the supply of Nd and Dy raw materials. In severe cases, exports may be restricted. Therefore, the use of rare earth permanent magnets should be reduced [10–13]. To reduce the dependence on rare earth permanent magnets, various motors that do not use rare earth permanent magnets, such as induction motors, synchronous reluctance motors (SynRMs) [14,15], and concentrated flux synchronous motors (CFSMs), have begun to be developed. Among the various motors that do not use rare earth permanent magnets, those using ferrite permanent magnets provide an optimal solution. The residual induction of ferrite permanent magnets is one-third that of rare earth permanent magnets [16]. On the other hand, the cost of ferrite permanent magnets is about one-tenth that of rare earth permanent magnets, and a stable supply of ferrite permanent magnets is easily obtained. Additionally, in high-temperature applications similar to those of EOPs, the low-temperature demagnetization characteristics of ferrite can be utilized to save magnet costs. As mentioned earlier, due to the lower residual induction of ferrite permanent magnets, it is necessary to increase the size of ferrite permanent magnets to meet the power and torque performance requirements [10–13,17–19]. This means an increase in the motor size. Therefore, selecting the optimal rotor magnet arrangement and structure is crucial. This paper analyzes various types of rotor arrangements with ferrite combinations and identifies the most suitable ferrite arrangement for an EOP rotor among the proposed rotor structures. It comprehensively compares the rotor shapes of SPM, IPM, and spoke-type IPM motors to establish design standards. This paper provides an important reference for the initial consideration of using ferrite magnet design methods for oil-cooled EOPs in EVs, the application scope, and the selection of ferrite rotor types, including a comparison of their advantages and disadvantages. The rest of this paper is organized as follows: Section 2 introduces the main parameters of ferrite motor rotors and the three analyzed rotor models. Section 3 compares the basic characteristics of each rotor and analyzes the torque and efficiency of the rotors. Finally, prototypes were manufactured based on the design structures. Section 4 shows a comparison of the model simulation and the experimental results. Concluding remarks are provided in Section 5.

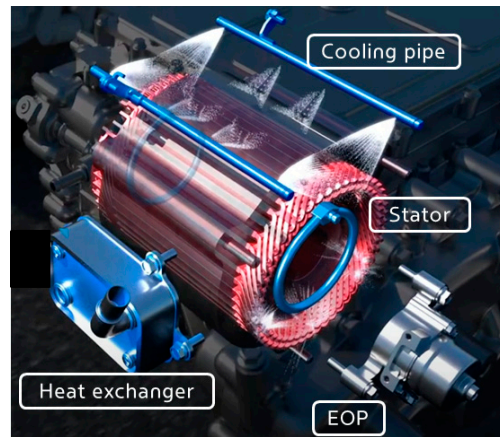


Figure 1. A diagram of the direct cooling of the end-winding in an oil-cooling drive motor for electric vehicles, reprinted with permission from Ref [20]. Copyright 2020 Hyundai-transys.

2. Electrometric Performances

2.1. Winding Factor

EV and HEV electronic oil pump motors generally use fractional slot concentrated windings (FSCWs). A typical characteristic of FSCW motors is the richness of the harmonic components, which greatly affects the various electromagnetic performances of the motor. In addition, the torque capacity of the motor is directly related to the fundamental winding factor. The winding factor of motors with different pole–slot combinations and double-layer windings is expressed as follows:

$$K_{wv} = \sin\left(\frac{vP}{Z} \pi\right) \frac{\sin(vp\alpha)}{N \sin\left(\frac{vp\alpha}{N}\right)} \tag{1}$$

In the formula, P is the number of pole pairs of the motor, $v = k/P$, k is the harmonic order, Z is the number of slots, $N = Z/r$, r is the greatest common divisor of the number of slots, poles, and phases, and α is the electrical angle between adjacent slots. From Formula (1), it can be seen that the winding factor of FSCW motors has periodicity and symmetry, which is the main reason for the generation of low-order harmonics and their irreducibility in FSCW motors. The winding factor can be used to derive the three-phase magnetomotive force (MMF) of the motor, as shown in Formula (2). Additionally, calculations were performed for three different pole–slot combinations (8/12, 10/12, and 14/12), and the results are shown in Figure 2.

$$K_v = \begin{cases} \frac{K_{wv}}{v} & v \neq (3 * j) / p \\ 0 & v = (3 * j) / p \end{cases} \quad j \in N^+ \tag{2}$$

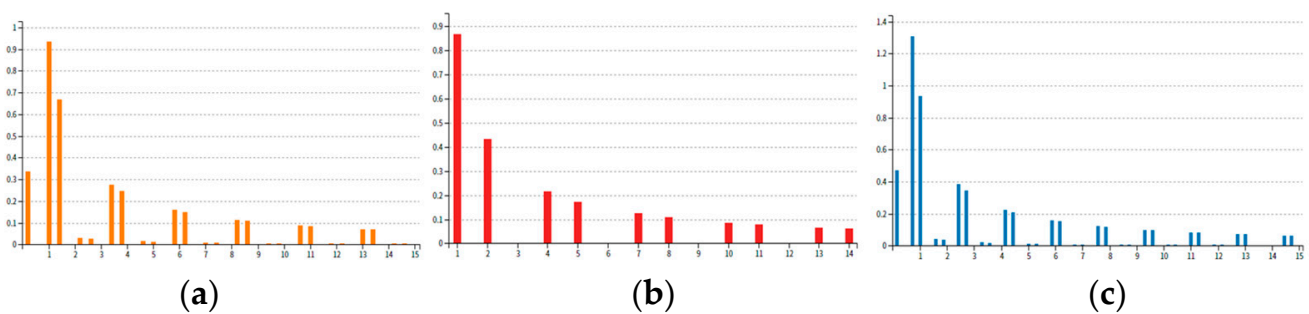


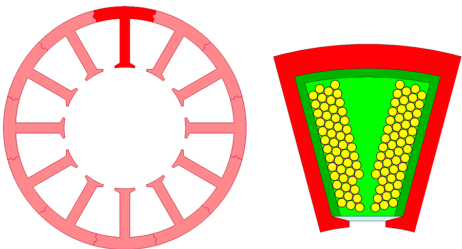
Figure 2. The three-phase MMF factor for the three pole–slot combinations, (a) 10/12, (b) 8/12, and (c) 14/12.

From Figure 2, it can be seen that all the motors contained rich harmonic components in the low-order harmonics. The 10/12 and 14/12 motors had larger subharmonics, which were the main reasons for motor losses and vibrations, while the 8/12 motor had no subharmonics. The over-harmonic amplitude of the 10/12 motor, except for the 7/5 harmonic amplitude, was smaller than that of the 14/12 motor, and the over-harmonic amplitude of the 12/8 motor was much smaller than that of the other two motors. However, the fundamental winding factor of the 10/12 and 14/12 motors was higher at 0.933, much higher than the 0.866 of the 8/12 motor, which helped to improve the output torque. Ultimately, after comprehensive consideration, we selected the 8/12 motor as the basic comparison model.

2.2. Stator Model for Analyzing Rotor Properties

Table 1 lists the specifications of the motor stator model used in this study. The rated DC voltage was 12 V. It is particularly noteworthy that the low magnetic flux density of the ferrite motor necessitated minimizing the back iron and tooth of the stator to provide the maximum slot area for the winding, thereby increasing the power density. Additionally, to increase the fill factor, a segmented stator was used. Finally, to secure the coil and for insulation, this design employed a 0.7 mm thick bobbin insulation.

Table 1. Main parameters of stator.

Item	Unit	Value	8/12 Stator, Slot of Stator
Outer and Inside Diameter	mm	60, 30	
Stack Length	mm	40	
Air Gap	mm	0.4	
Coil Size (bare)	mm	0.71	
No. of Turns, Strands	-	52, 1	
Phase Resistance@20 degC	Ω	0.076	
Fill Factor	%	43	
Bobbin Insulation Thickness	mm	0.7	

2.3. Analysis Models of Motor Rotor

To analyze the relationship between the characteristics of various motors and rotor shapes, the outer diameter of each rotor was fixed to ensure the same conditions and minimize the number of variables. Additionally, the arrangement of the rotor magnets was adjusted to standardize the size and shape of the stator and winding, allowing for the analysis of characteristics under similar conditions. To ensure the accuracy of the analysis using different magnet arrangements and rotor shapes, the typical rotor shape and ratio of the EOP were maintained as much as possible. The final design and the main parameters are listed in Table 2.

Table 2. Comparison of rotors.

Item	Unit	Model 1	Model 2	Model 3
No. of Magnet Poles	-		8	
PM Grade			NMF-12E	
Outer and Inside Diameter	mm	28.6, 9, sleeve (0.3)	29.2, 11	29.2, 9
Stack Length	mm		40	
Magnet Thickness	mm		4.5	
Magnet Weight	g	58.0	51.8	46.3

Generally, due to the low residual magnetic flux density of ferrite magnets, larger magnets must be used to achieve a greater torque density in EOPs. In the case of the IPM-type rotor, larger magnets could not be used structurally because barriers and ribs had to be added. Additionally, to obtain demagnetization characteristics and compare similar performances, the magnet thickness was 4.5 mm. Furthermore, for the SPM-type rotor, a sleeve had to be added to the outer layer of the motor rotor to prevent the magnets from flying off during high-speed rotation. In this paper, the sleeve used was made of stainless steel with a thickness of 0.3 mm. For the spoke-type IPM rotor, the inner diameter of the rotor was particularly important because the magnetization direction of the magnets was not radial towards the air gap but tangential to the air gap. Therefore, the iron core connection between the N and S poles needed to maximize the rotor's inner diameter to minimize it, thereby minimizing the magnetic leakage. Finally, all optimized rotors had to meet the rotational strength requirements. The different shapes of the ferrite magnet rotors were as shown in Figure 3.

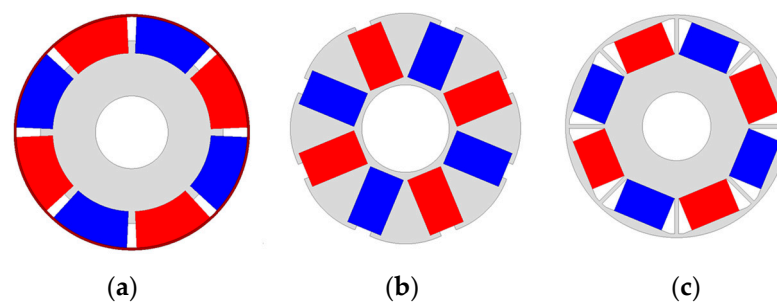


Figure 3. Three different shapes of ferrite magnet rotors: (a) model 1 (SPM with sleeve), (b) model 2 (spoke-type IPM), (c) model 3 (IPM).

3. Comparison of Electromagnetic Performance

3.1. No-Load Analysis of Three Models

The no-load back electric motive force (B-EMF) is an important parameter for analyzing the motor flux and power density. Figure 4a shows the peak line-to-line B-EMF at different speeds. It was found that due to the pole piece structure between the ferrite magnet and air gap of the IPM model, there was leakage flux, resulting in a low no-load back EMF. Meanwhile, although the spoke-type IPM also had a pole piece structure, the magnets caused the magnetic flux to converge in their arrangement, increasing the air gap flux density. In the SPM structure, the ferrite magnet was closest to the air gap, resulting in minimal leakage flux. Even with a sleeve structure, it could still achieve a high air gap flux density. Under the conditions of 1000 rpm and an ambient temperature of 20 degrees, the maximum phase-to-phase B-emfs for model 1, model 2, and model 3 were 2.13 V, 2.19 V, and 0.69 V, respectively. Figure 4b shows the B-EMF Fourier transform (FFT) analysis results. From the FFT analysis, under the same speed and temperature conditions, the fundamental B-EMFs for model 1, model 2, and model 3 were 2.13 V, 2.18 V, and 0.66 V, respectively. It is evident that these values are almost the same as the phase-to-phase back EMF, indicating that the harmonic components were very low. The total harmonic distortion (THD) was approximately 4.93%, 5.37%, and 9.08%, respectively. Additionally, Figure 4c shows that the cogging torque of each motor was calculated to be 0.054 Nm, 0.055 Nm, and 0.009 Nm, respectively.

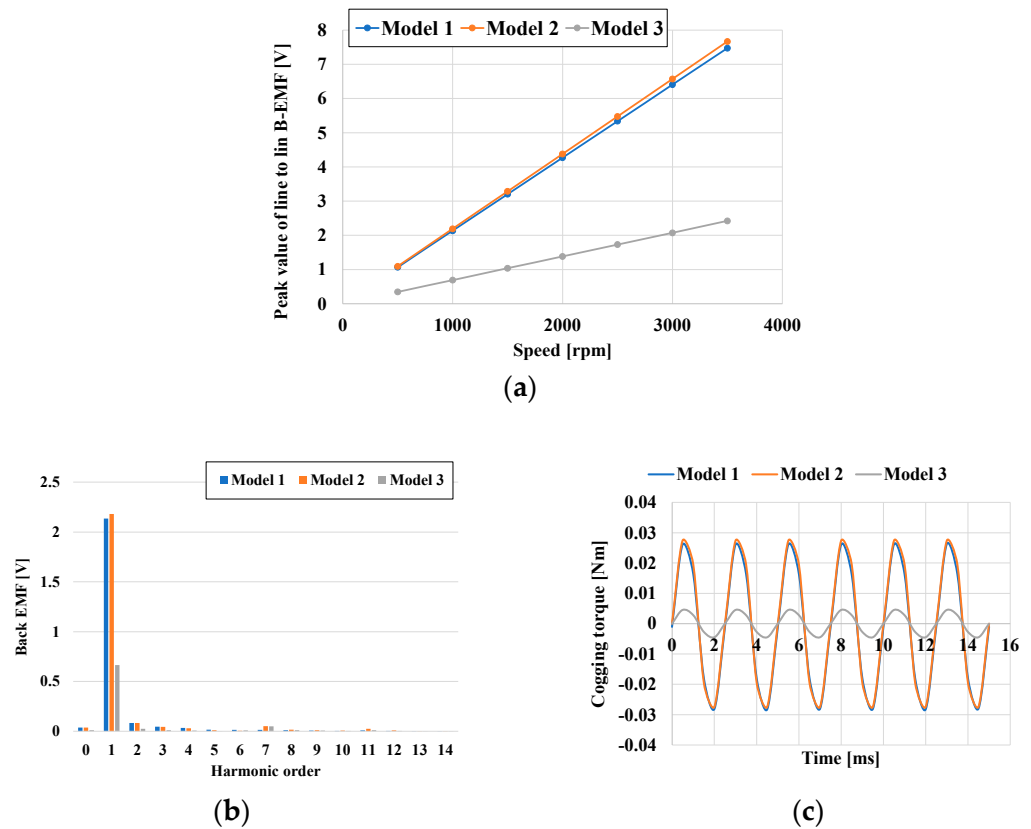


Figure 4. (a) The phase B-EMF of the three models. (b) The FFT analysis of the three models. (c) The cogging torque for the three models.

3.2. Speed–Torque and Speed–Efficiency Analysis

Another type of electromagnetic analysis was performed by applying a constant current at different speeds. Considering the B-EMF, the traction motor required a cooling flow and pressure for the oil pump, with the analysis range being up to the maximum speed of 3500 rpm. Initially, the analysis used the magnet torque without controlling the phase angle. It is well known that the reluctance in IPM motors, i.e., the salient poles, generates additional torque components. The spoke-type IPM, being a salient pole, increased the torque for a given current amplitude through phase angle control. It was found that the maximum torque occurred for the IPM at a current phase of 35–45°, for the spoke-type IPM at 15–20°, and for the SPM, which had no salient pole structure, the maximum current phase angle was generally 0°. This study conducted comparative analyses using different current phase angles in each motor to examine the characteristics of the maximum torque. As shown in Figure 5, to analyze the effects of the d-axis and q-axis, the analysis indicated that under the same current input, the spoke-type IPM configuration had the highest torque (0.46 Nm) due to its large magnet volume and effective magnetic flux generation. In contrast, the ferrite magnet in the IPM had the smallest effective magnetic flux. Figure 6 compares the magnetic field densities of the different models. It is important to note that not only was the rotor lamination significantly different, but the stator core saturation of the models also varied under load operation (as seen in Figure 6).

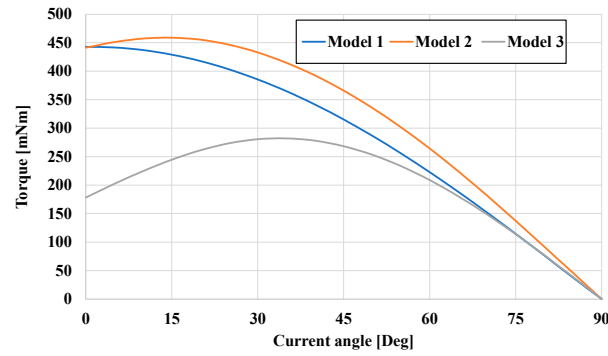


Figure 5. FEM torque value at different current angles (phase current Ia: 12 arms).

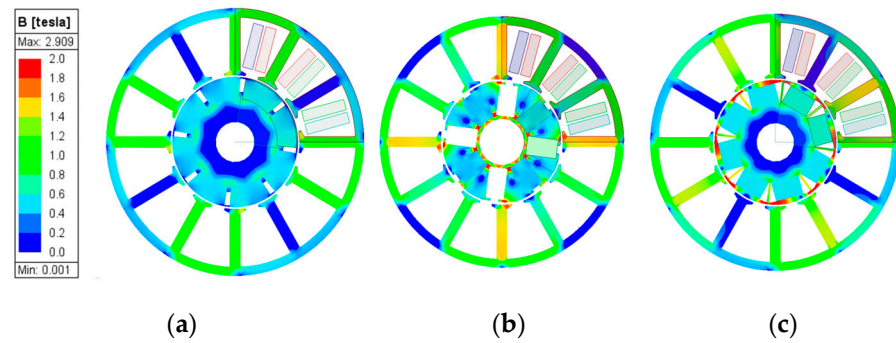


Figure 6. Cross section and flux density distributions of three models in MPTA condition. (a) Model 1, load condition (Ia: 12 arms; β : 0°). (b) Model 2, load condition (Ia: 12 arms; β : 15°). (c) Model 3, load condition (Ia: 12 arms; β : 35°).

Figure 7 compares the torque and power characteristics at different rotational speeds. The analysis shows that model 2 had the highest basic speed torque. This is because, as mentioned earlier, the ferrite magnetic flux was concentrated, and there was minimal magnetic leakage. The air gap magnetic flux density of model 2 was very high.

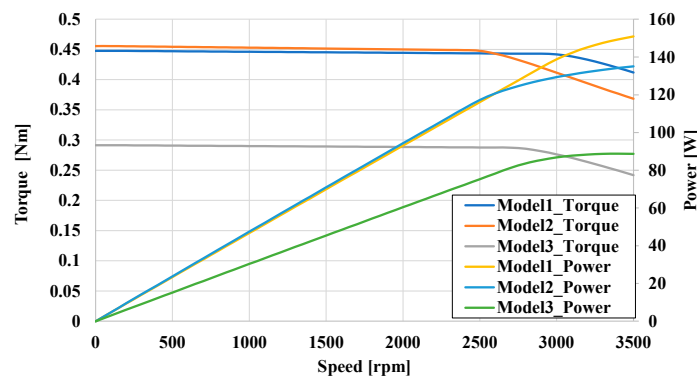


Figure 7. Comparison of torque and power according to speed.

Model 1 also had a high torque density. Due to the proximity of the ferrite to the air gap, the air gap magnetic flux density was increased. Additionally, even within the range of high-speed magnetic field weakening and Maximum Torque Per Volt (MTPV) control, model 1 did not exhibit a rapid torque drop in the high-speed range (2700–3500 r/min). This is attributed to the high initial basic speed and the low residual magnetic field strength of the ferrite, making it easy to modulate weak magnetic control. Finally, the power curve shows that model 1 had the highest power.

3.3. A Comparison of the Efficiency Maps and WLTP Class 3 Driving Cycle

Figure 8 shows the electric efficiency maps of the three models. Since model 3 did not meet the maximum torque performance requirements, this chapter mainly considers the efficiency characteristics of model 1 and model 2. It was found that due to the higher torque density of model 2, model 2 had higher efficiency in the low-speed, high-torque region where the copper loss was significant. By referring to the diagram of the magnetic flux density under a load (Figure 6), it can be seen that model 1 had a lower magnetic saturation density, resulting in lower iron loss compared to model 2. Therefore, model 1 had greater efficiency in the high-speed, low-torque region.

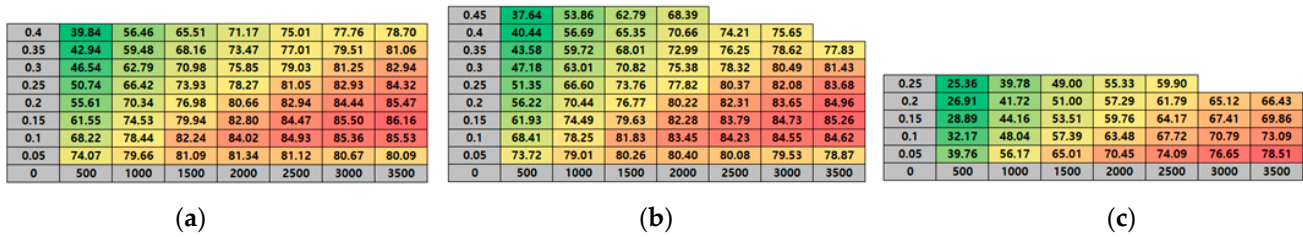


Figure 8. Efficiency maps of three models: (a) model 1; (b) model 2; (c) model 3.

To further discuss the performance of the EOP in terms of the EV traction motor system efficiency, it was necessary to comprehensively consider the operating power points of the EOP in the EV traction motor. These power points also needed to refer to the global driving cycle standard tests for electric vehicles, such as the WLTP, NEDC, and US06. It should be noted that the EOP speed needed to be determined by referring to the motor temperature (usually the end-winding temperature) and the traction motor circulating oil temperature. At the same time, power tests on the EOP needed to be conducted under different oil circulation system pressures and flow rates. Based on the test results, a three-dimensional lookup table (EOP speed/oil flow/oil temperature) was used to find the output power at each operating point during the endurance test. Finally, the efficiency of the rotary pump was added to obtain the power point of the EOP motor. Figure 9 shows the operating points of an EV oil-cooled traction motor EOP under the WLTP class 3 driving cycle, which is a specific category within the global WLTP testing program designed for high-performance light-duty vehicles, particularly EVs with a top speed exceeding 130 km/h [21–24].

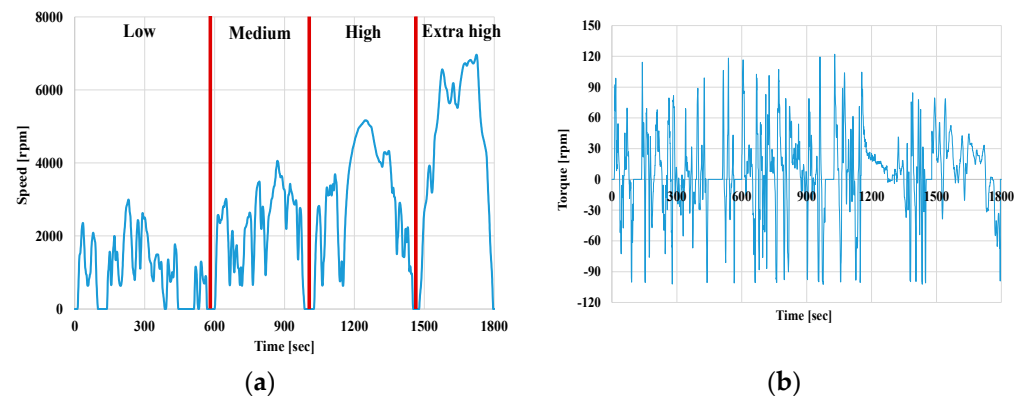


Figure 9. (a) The motor speed and (b) absolute load torque over the WLTP class 3 driving cycle, reprinted from Ref. [23].

The rotational speed of the target traction motor and the EOP motor, as well as the torque curves, are shown in Figure 10. It can be seen that during the initial cycle phase (low and medium WLTP range), the EOP motor’s operating conditions were not severe. The temperature rises of the traction motor coils and the oil temperature increase in the oil

cooling system were not significant. Therefore, during the initial cycle phase, there was no need to significantly increase the oil flow rate, and the required torque of the EOP motor did not increase much. However, during the high-speed cycle phase (high and extra-high WLTP range), the motor coils heated up rapidly under high-speed operation, resulting in a significant increase in the required flow rate, which led to an increase in the EOP motor speed and torque. Next, by considering cold-start and hot-start environments, two different operating points of the EOP at 25 °C and 65 °C were extracted (the temperatures refer to the traction motor cooling inlet oil temperature; in the experiment, a fixed chiller was usually used to set a constant oil inlet temperature, which was then supplied to the traction motor). It can be seen that in a high-oil-temperature environment, the command required the EOP to operate at a high speed; therefore, the EOP operating speed was much higher. However, in a high-oil-temperature environment, the viscosity of the oil decreased, and compared to a low-oil-temperature environment, the required EOP motor torque was lower. Figure 11a shows the required operating points under the maximum torque speed of the three EOP models in WLTP class 3. It can be seen that all possible operating points of the WLTP class 3 driving cycle are within the torque–speed curve specified by model 1 and 2. However, the maximum torque margin of model 3 is insufficient (unable to meet the requirements of a below-zero oil temperature and certain extreme operating conditions).

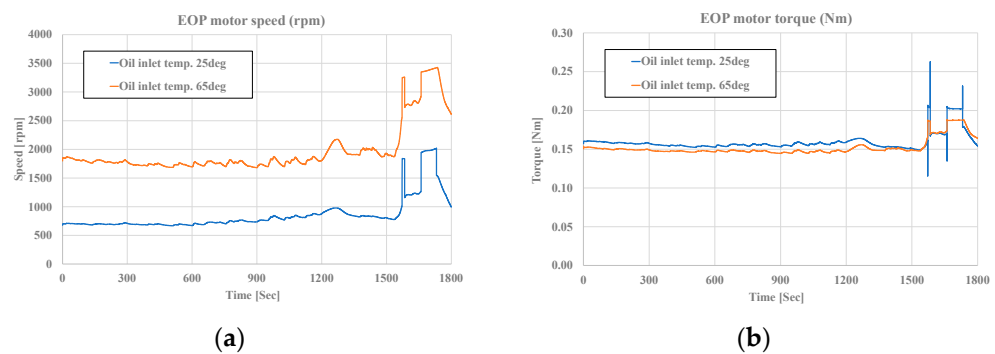


Figure 10. (a) The EOP motor speed and (b) absolute EOP motor torque over the WLTP class 3 driving cycle.

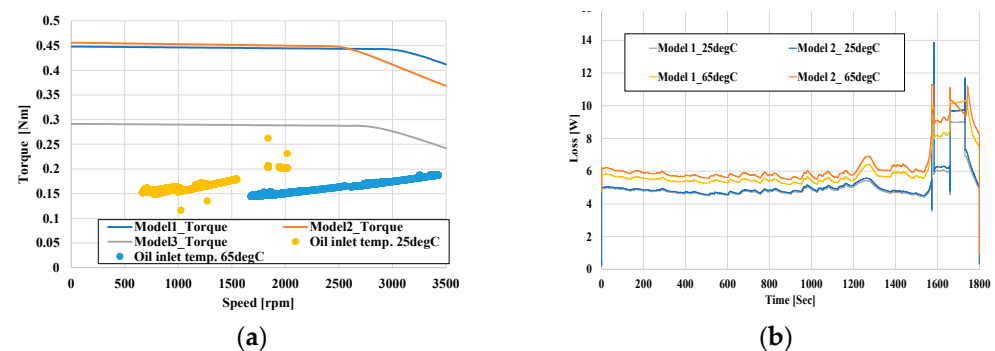


Figure 11. (a) EOP motor specification for peak torque versus speed characteristics (all models); (b) loss over WLTP class 3 for model 1 and model 2.

Finally, the motor's total loss is shown in Figure 11b. The motor's losses included iron losses, copper losses, and permanent magnet eddy current losses. These results were obtained from a steady-state FEM analysis conducted every 0.1 s. In a low-oil-temperature environment (25 °C), the losses of model 1 and model 2 exhibited similar performance during the initial cycle phase, representing urban driving conditions (low and medium WLTP range). However, during simulated suburban and high-speed driving (starting from 1300 s), the losses of model 2 were higher than those of model 1. As previously mentioned,

in the high-speed range, model 2 had higher iron losses due to a higher magnetic flux and magnetic saturation. Therefore, their energy consumption increased rapidly in the high and extra-high WLTP range. In a high-oil-temperature environment (65 °C), the losses of model 1 were lower than those of model 2 across the entire range of the WLTP. This is also because, in a high-temperature environment, the oil pump needs to rotate at a high speed across the entire WLTP range. The energy consumption in each range is confirmed in Table 3.

Table 3. The energy loss over WLTP class 3 for the EOP models.

Item	Unit	Model 1		Model 2	
		25 °C	65 °C	25 °C	65 °C
WLTP low-range loss	Wh	0.798	0.924	0.808	0.983
WLTP medium-range loss		0.529	0.602	0.536	0.639
WLTP high-range loss		0.622	0.717	0.635	0.766
WLTP extra-high-range loss		0.589	0.754	0.618	0.800

4. Results of Experiment

Through the analysis in the previous chapter, comparing model 2 and model 3, we found that model 1 had the greatest advantages in terms of the power density, efficiency, and ease of manufacturing (models 2 and 3 generally magnetized after insertion). To verify the design results, an SPM prototype was made. Figure 12 shows the stator and rotor of the SPM prototype. Figure 13a shows the experimental and simulated values of the no-load line induced voltage at a speed of 1000 r/min. The experimental value of the no-load line induced voltage was 1.47 Vrms, and the simulated value was 1.51 Vrms. Additionally, a comparison of the measured and simulated values of the cogging torque is reflected in Figure 13b. Finally, a comparison of the experimental and simulated efficiencies under the load torque is shown in Table 4. All experimental data indicated that the two values were relatively close.

Table 4. Efficiency comparison at rated power point.

Item	FEM	Experiment	Error
Base speed	3200 rpm	3194 rpm	0.18%
Torque	0.348 Nm	0.359 Nm	3.0%
Power	116.5 W	120.3 W	3.5%
Efficiency	80.2%	80.0%	0.2%

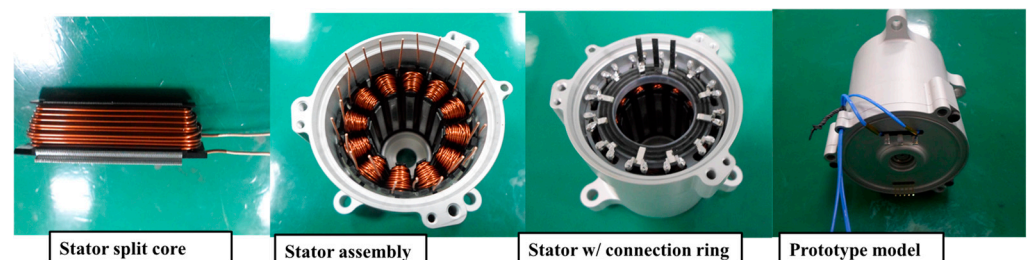


Figure 12. The prototype of the SPM with a ferrite magnet for the EOP.

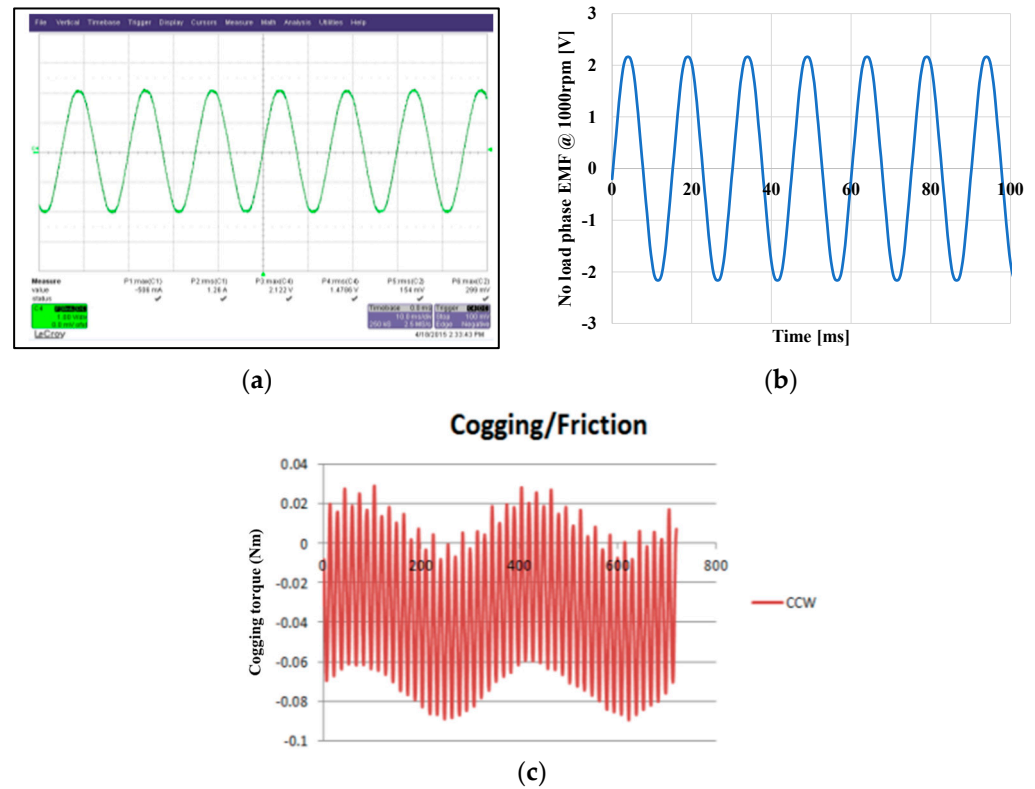


Figure 13. Experiment and simulation results of no-load line induced voltage at 1000 r/min. (a) Experiment. (b) Simulation. (c) Experiment results of cogging torque, reprinted with permission from Ref. [25]. Copyright 2020 IEEE.

5. Conclusions

This paper presents the optimal design scheme for the latest pure electric drive cooling EOP, a ferrite magnet rotor motor, which can provide high efficiency, a high torque density, and a low torque ripple in EOP applications. Combined with the cooling control scheme, the proposed Fe-PM SPM rotor achieved the highest system efficiency. Finally, the no-load and load operation performances were obtained through experimental measurements. Based on the comparison of the simulation and experimental results, the following conclusions were drawn:

- (1) The air gap magnetic density of the ferrite magnet rotor motor is very low. Therefore, when designing such a motor, it is necessary to select a design with the maximum air gap magnetic density, minimize magnetic leakage as much as possible, and concentrate the magnetic density of the magnets. Therefore, rotor structures similar to the SPM and spoke-type IPM can meet the design requirements.
- (2) The IPM structure is very unsuitable for ferrite rotors, as its construction cannot maximize the magnet area, the magnets are far from the air gap, and the structure retains ribs and bridges, which will inevitably cause magnetic leakage, thereby reducing the power density and motor efficiency.
- (3) When analyzing the system efficiency, it is necessary to consider the efficiency of the EOP motor at high operating points, considering the high cooling oil temperature. The system will require high flow rates and high EOP operating speeds. Therefore, although increasing the air gap magnetic density is particularly important, the magnetic density of the stator core also needs attention. It is necessary to improve the magnetic density of the core to reduce iron loss and enhance the high-speed efficiency of the ferrite motor.

Finally, the SPM-type motor (model 1) achieved a higher torque density by configuring more ferrite magnets, but it requires additional ferrite magnet material and a sleeve structure, which may lead to higher costs. Considering the fluctuations in magnet prices and the impact of EOP losses on the electric vehicle system, future research should delve deeper into the trade-offs between the motor manufacturing complexity, motor cost, and system performance.

Funding: This research received no external funding.

Data Availability Statement: The original contributions presented in the study are included in the article, further inquiries can be directed to the corresponding author.

Conflicts of Interest: The author is an employee of Hwaseong Powertrain R&D Center, Hyundai-Transys. The paper reflects the views of the scientists, and not the company.

References

1. Rostek, E.; Babiak, M.; Wróblewski, E. The Influence of Oil Pressure in the Engine Lubrication System on Friction Losses. *Procedia Eng.* **2017**, *192*, 771–776. [[CrossRef](#)]
2. Doikin, A.; Habib Zadeh, E.; Campean, F.; Priest, M.; Brown, A.; Sherratt, A. Impact of Duty Cycle on Wear Progression in Variable-displacement Vane Oil Pumps. *Procedia Manuf.* **2018**, *16*, 115–122. [[CrossRef](#)]
3. Kim, Y.; Lee, J.; Jo, C.; Kim, Y.; Song, M.; Kim, J.; Kim, H. Development and control of an electric oil pump for transmission-based hybrid electric vehicles. *IEEE Trans. Veh. Technol.* **2011**, *60*, 1981–1990. [[CrossRef](#)]
4. Tang, X.; Zhang, D.; Liu, T.; Khajepour, A.; Yu, H.; Wang, H. Research on the energy control of a dual-motor hybrid vehicle during engine start-stop process. *Energy* **2019**, *166*, 1181–1193. [[CrossRef](#)]
5. Fletcher, T.; Thring, R.; Watkinson, M. An Energy Management Strategy to concurrently optimise fuel consumption & PEM fuel cell lifetime in a hybrid vehicle. *Int. J. Hydrogen Energy* **2016**, *41*, 21503–21515.
6. Choi, C.; Kim, J. Model-Based Angular Position Sensor less Drives of Main Electric Oil Pumps for e-Axles in HEV and BEV. *Energies* **2024**, *17*, 4962. [[CrossRef](#)]
7. Huang, J.; Naini, S.S.; Miller, R.; Rizzo, D.; Sebeck, K.; Shurin, S.; Wagner, J. A Hybrid Electric Vehicle Motor Cooling System—Design, Model, and Control. *IEEE Trans. Veh. Technol.* **2019**, *68*, 4467–4478. [[CrossRef](#)]
8. Ghahfarokhi, P.S.; Podgornovs, A.; Kallaste, A.; Cardoso, A.J.M.; Belahcen, A.; Vaimann, T. The oil spray cooling system of automotive traction motors: The state of the art. *IEEE Trans. Transp. Electrification* **2023**, *9*, 428–451. [[CrossRef](#)]
9. Huynh, T.A.; Hsieh, M.-F. Improvement of Traction Motor Performance for Electric Vehicles Using Conductors with Insulation of High Thermal Conductivity Considering Cooling Methods. *IEEE Trans. Magn.* **2021**, *57*, 8202405. [[CrossRef](#)]
10. Guo, S.; Su, X.D.; Zhao, H. Optimal Design of an Interior Permanent Magnet Synchronous Motor for Electric Vehicle Applications Using a Machine Learning-Based Surrogate Model. *Energies* **2024**, *17*, 3864. [[CrossRef](#)]
11. Liu, H.-C.; Kim, I.-G.; Oh, Y.J.; Lee, J.; Go, S.-C. Design of permanent magnet-assisted synchronous reluctance motor for maximized Back-EMF and torque ripple reduction. *IEEE Trans. Magn.* **2017**, *53*, 1–4. [[CrossRef](#)]
12. Sone, K.; Takemoto, M.; Ogasawara, S.; Takezaki, K.; Akiy, H. A ferrite PM In-Wheel motor without rare earth materials for electric city commuters. *IEEE Trans. Magn.* **2012**, *48*, 2961–2964. [[CrossRef](#)]
13. Obata, M.; Morimoto, S.; Sanada, M.; Inoue, Y. Performance of PMA SynRM with ferrite magnets for EV/HEV applications considering productivity. *IEEE Trans. Ind. Appl.* **2014**, *50*, 2427–2435. [[CrossRef](#)]
14. Liu, H.C.; Lee, J. Optimum Design of an IE4 Line-Start Synchronous Reluctance Motor Considering Manufacturing Process Loss Effect. *IEEE Trans. Ind. Electron.* **2018**, *65*, 3104–3114. [[CrossRef](#)]
15. Wang, Y.; Bianchi, N.; Qu, R. Comparative study of non-rare-earth and rare-earth PM motors for EV applications. *Energies* **2022**, *15*, 2711. [[CrossRef](#)]
16. Park, J.-H.; Jung, K.-T.; Jung, Y.-H.; Lim, M.-S.; Yoon, M.-H.; Hong, J.-P.; Jung, J.-W. Design and Verification for the Torque Improvement of a Concentrated Flux-Type Synchronous Motor for Automotive Applications. *IEEE Trans. Ind. Appl.* **2019**, *55*, 3534–3543. [[CrossRef](#)]
17. Kalluf, F.J.H.; Isfanuti, A.S.; Tutelea, L.N.; Moldovan-Popa, A.; Boldea, I. 1-kW 2000–4500 r/min ferrite PMSM drive: Comprehensive characterization and two sensorless control options. *IEEE Trans. Ind. Appl.* **2016**, *52*, 3980–3989. [[CrossRef](#)]
18. Barcaro, M.; Bianchi, N. Interior PM machines using ferrite to replace rare-earth surface PM machines. *IEEE Trans. Ind. Appl.* **2014**, *50*, 979–985. [[CrossRef](#)]
19. Jung, Y.; Park, M.; Kim, K.; Chin, J.; Hong, J.; Lim, M. Design of high-speed multilayer IPMSM using ferrite PM for EV traction considering mechanical and electrical characteristics. *IEEE Trans. Ind. Appl.* **2021**, *57*, 327–339. [[CrossRef](#)]

20. Hyundai-Transys. [ENG] Hyundai Transys Electric Powertrain Solution. *YouTube*. 2020. Available online: <https://www.youtube.com/watch?v=h1c-ieAuV7c> (accessed on 22 October 2020).
21. Hwang, S.-W.; Ryu, J.-Y.; Chin, J.-W.; Park, S.-H.; Kim, D.-K.; Lim, M.-S. Coupled Electromagnetic-Thermal Analysis for Predicting Traction Motor Characteristics according to Electric Vehicle Driving Cycle. *IEEE Trans. Veh. Technol.* **2021**, *70*, 4262–4272. [[CrossRef](#)]
22. Mahmouditabar, F.; Baker, N.J. Design Optimization of Induction Motors with Different Stator Slot Rotor Bar Combinations Considering Drive Cycle. *Energies* **2024**, *17*, 154. [[CrossRef](#)]
23. Liu, H.-C.; Park, J.S.; An, I.H. Design, Analysis, and Comparison of Electric Vehicle Drive Motor Rotors Using Injection-Molded Carbon-Fiber-Reinforced Plastics. *World Elec. Veh. J.* **2024**, *15*, 283. [[CrossRef](#)]
24. Muazzam, H.; Ishak, M.K.; Hanif, A.; Bhatti, A.I. Compensating Thermal Derated Torque of IPMSM Centric Electric Vehicles. *IEEE Access* **2022**, *10*, 22468–22480. [[CrossRef](#)]
25. Liu, H.-C.; Kim, H.; Jang, H.; Jang, I.-S.; Lee, J. Ferrite PM Optimization of SPM BLDC Motor for Oil-Pump Applications According to Magnetization Direction. *IEEE Trans. Appl. Supercond.* **2020**, *30*, 2977615. [[CrossRef](#)]

Disclaimer/Publisher’s Note: The statements, opinions and data contained in all publications are solely those of the individual author(s) and contributor(s) and not of MDPI and/or the editor(s). MDPI and/or the editor(s) disclaim responsibility for any injury to people or property resulting from any ideas, methods, instructions or products referred to in the content.